Electrochemical Properties of Transparent Conducting Films of Tantalum-Doped Titanium Dioxide

Hana Krysova[1], Piero Mazzolini[2,3], Carlo S. Casari[2,3], Valeria Russo[2], Andrea Li Bassi[2,3], Ladislav Kavan[1]

[1]J. Heyrovsky Institute of Physical Chemistry ASCR, v.v.i., Dolejskova 2155/3, 182 23 Prague 8, Czech Republic

[2]Department of Energy, Politecnico di Milano, via Ponzio 34/3, Milano, Italy

[3]Center for Nano Science and Technology, IIT@PoliMI, Via Pascoli 70/3, I-20133 Milano, Italy

E-mail: ladislav.kavan@jh-inst.cas.cz

ABSTRACT

Highly conducting, optically transparent Ta-doped TiO_2 (anatase) thin films are grown on ordinary soda-lime glass substrate by pulsed-laser deposition. They exhibit quasi-reversible cyclic voltammograms of $Fe(CN)_6^{3-/4-}$ and dimethylviologen redox couples, mimicking the electrochemical activity of F-doped SnO_2 (FTO). Hence, our Ta-doped titania films can prospectively replace FTO, e.g. in homo-junction dye-sensitized and perovskite solar cells. However, these films are idle for the $Ru(bpy)_3^{2+}$ oxidation, which is attributed to the space-charge barrier. The flatband potential of our Ta-doped TiO_2 is comparable to that of undoped reference film and/or the pristine anatase single-crystal electrode. Our films show photoelectrochemical activity upon irradiation with UV light at potentials positive to flatband. The photocurrents decrease proportionally to the increase of Ta-content. The Li-insertion ability analogously decreases with the increasing Ta-content. This is attributed to the positive charge of Ta^{5+} cations which occupy the Ti^{4+} sites in anatase lattice and thus impede the Li^+-transport. Consistent with the quasi-metallic nature of our films, the Li-extraction peak in cyclic voltammograms shows no cut at larger potentials.

Keywords: titanium dioxide, tantalum doping, electrochemistry, UV-photoelectrochemistry, Li-insertion

1. INTRODUCTION

Transparent conducting oxides, such as indium-tin oxide (ITO) and F-doped SnO_2 (FTO) are widely used in electrochemistry, and in related applications like in dye-sensitized solar cell (DSC) [1,2] and photoelectrochemical water splitting for solar fuel generation [3]. However, there is a strong demand for their replacement by cheaper materials [4]. Other issues specific for DSC applications are the thermal instability of ITO [5] and the formation of a Schottky barrier at the heterojunction photoanode interface of TiO_2 with both ITO [5] and FTO [6,7]. It stems from the fact that the Fermi level of TiO_2 is higher than that of ITO/FTO prior to contact of the materials. This is particularly important when a dense titania layer [6,7] is deposited on top of FTO to prevent recombination [8,9]. These layers are prepared by various techniques [6–10], including electrochemical methods [8,10]. The control of energy level alignment throughout the interfaces is important for photovoltaic devices such as solid state DSCs and perovskite solar cells [11]. For instance, a homo-junction FTO/SnO_2 electrode [12] enables barrier-free alignment with certain perovskites [13]. However, a barrier-free titania homo-junction electrode, employing solely doped TiO_2 as an electron collecting terminal, was not yet reported, to the best of our knowledge.

Nb-doped [7] and Ta-doped [14] dense TiO_2 deposited on top of FTO improve the performance of DSC due to enhanced charge collection efficiency. Similar improvement was reported for Ta-doped TiO_2 which was deposited as the last over-layer on top of mesoporous TiO_2 [15]. Ta-doped TiO_2 nanotubes [16] or other Ta-doped nanostructures [17–19] were used as the photoanode material, too. Interestingly, even pure Ta_2O_5 (band gap of ca. 4 eV) is applicable as a DSC photoanode, but with very low efficiency. Pure Ta_2O_5 has a lower conduction band (CB) edge than TiO_2 (ca. -4.6 eV/vacuum) which obviously decreases the attainable voltage of DSC [20]. On the other hand, a composite Ta_2O_5/TiO_2 behaved considerably better in DSCs [19]. Ta-doped TiO_2 nanotubes also showed improved water splitting ability as compared to pure TiO_2 [21].

A purely titania-based 'transparent metal' with resistivity as low as $(2-3) \cdot 10^{-4}$ $\Omega \cdot cm$ was demonstrated through Nb-doping [22,23] and Ta-doping [24]. These doped titania layers are degenerate n-type semiconductors thanks to an efficient electron release from the pentavalent

dopant [23,25]. The Ta^{5+} ions occupy Ti^{4+} sites in the anatase lattice and sometimes also concomitant doping by Ti^{3+} and Ta^{5+} was observed [26]. Ta-doping is favored over Nb-doping by higher Ta solubility in TiO_2, higher electron mobility and by retardation of anatase/rutile transformation [26]. Compared to ITO, the doped TiO_2 provides higher refractive index, higher transmittance in the IR-region, and good stability in reducing atmosphere [23]. Highly-conductive titania can be prepared through sputtering or pulsed-laser deposition (PLD) [23,27–29]. Sporadic reports about other fabrication techniques, such as chemical vapor deposition, show that these Ta-doped TiO_2 films are less conducting ($\approx 10^{-3}$ $\Omega \cdot cm$) [26]. Some of us have recently optimized PLD deposition of polycrystalline Ta-doped TiO_2 on glass substrates, and investigated the role of the deposition conditions and annealing atmosphere [27,28] on the electrical, optical [28] and vibrational [29] properties. In particular, the obtained carrier density is influenced not only by the dopant (Ta) content, but also by the presence of intrinsic defects in the crystalline structure. This is controlled in a complicated way by the oxygen partial pressure during deposition and by the vacuum-annealing conditions. The explanation is still debated [27–29] and involves the formation of 'electron killer' defects such as Ti vacancies or O interstitials.

As mentioned above, the replacement of FTO by metal-like conducting TiO_2 for a homo-junction electron-collector in DSC (i.e. the 'all-TiO_2 photoanode') is a straightforward challenge. The first step in this effort is obviously the exploration of electrochemical properties of this material, which is the central motivation of our study. We are not aware of any similar work on electrochemical properties of Ta-doped TiO_2 electrodes. To fill the gap, we characterize here the electrochemical performance of Ta-doped TiO_2 films obtained by PLD, focusing on voltammetric response of model redox couples, electrochemical impedance spectroscopy, photoelectrochemistry under band-gap excitation and the Li-insertion electrochemistry.

2. EXPERIMENTAL SECTION

2.1. Preparation of electrodes

TiO_2 thin films with the nominal doping amount (Ta content 1, 5, and 10 atomic %) were deposited by PLD on soda-lime glass substrates at room temperature using a lamp-pumped Q-switched Nd:YAG pulsed laser (fourth harmonic, $\lambda = 266$ nm, repetition rate 10 Hz, pulse

duration ≈ 6 ns, target-to-substrate distance = 50 mm). Films with about 1% Ta content were obtained by uniform ablation of TiO_2 target (powder purity 99.9%) partially covered with Ta metallic wires, so that a fraction of the surface corresponding to roughly 1% Ta with respect to Ti is covered. Pure TiO_2 films were grown starting from the same ceramic target, while Ta-doped films with 5 and 10% Ta content were obtained by ablating sintered Ta_2O_5:TiO_2 targets (molar ratios of 0.025:0.975 and 0.05:0.95 corresponding to 5% and 10% nominal Ta content respectively, powder purity 99.99%). Different oxygen partial pressures (in the range of 1-2 Pa) have been used to tune the film properties, as discussed in [28]. The pulsed laser energy density on the target was typically 1.15 J/cm^2. The PLD process was always followed by ex-situ annealing performed in air or in vacuum (p < 4×10^{-5} Pa) at 550°C with a dwell time of 60 min in a homemade heating system and heating/cooling ramp of 10 K/min.

Each electrode was prepared from a sample layer with dimensions approx. 5 x 10 mm^2. Contact was made by Ga-In alloy to Cu-wire and protected by TorrSeal epoxy. In some cases, the contact was made simply by Ag-epoxy or by ultrasonic solder (Cerasolazer CS186). The exposed area was defined by TorrSeal encapsulation between 0.16 to 0.36 cm^2.

2.2. Characterization of electrodes

Film thickness was evaluated by scanning electron microscopy (SEM, Zeiss SUPRA 40 field-emission microscope) on samples grown on silicon. Layer thickness of most samples was 150 nm, sometimes also larger thicknesses (290 nm and 500 nm) were grown (see Fig. S1 in Supporting Info). The crystalline structure and its dependence on the deposition/annealing conditions have been investigated in previous works [27–29] by a combination of X-ray diffraction and Raman spectroscopy; in this work we checked the crystalline phase by micro-Raman measurements (Renishaw In Via spectrometer with Ar^+ laser, λ = 514.5 nm, power on sample 1 mW). Example spectrum is shown in Fig. S2 (Supporting Info). The electrical characterization was performed in the 4-point probe configuration with a Keithley K2400 Source/Measure Unit as a current generator (from 100 nA to 10 mA), an Agilent 34970A voltage meter, and a 0.57 T Ecopia permanent magnet for Hall measurements.

Electrochemical experiments were carried out in a one-compartment cell using Autolab PGstat-30 (Metrohm) with the FRA module. The reference electrode was Ag/AgCl (sat. KCl) for experiments in aqueous electrolyte solutions, and Li-metal for aprotic media. The Li insertion

experiments were carried in 1 M $LiClO_4$ in (1/1 w/w) mixture of ethylene carbonate (EC) + dimethoxy ethane (DME) electrolyte solution. In this case, the reference and counter electrodes were from Li metal, hence, potentials were quoted against the Li/Li^+ reference electrode in this medium. The electrolyte solutions were purged with argon, and the measurement was carried out in a glove box under Ar atmosphere. A commercial FTO glass, TEC 15 from Libbey-Owens-Ford, was used as a reference material. Its sheet resistance was 15 Ohm/sq (declared by the manufacturer; own measurement provided 13.4 Ohm/sq), visible-light transmittance 82-85 %, layer thickness ca. 500 nm). Electrolytes, solvents and redox-active molecules were of the standard quality (p.a. or electrochemical grade) purchased from Aldrich or Merck and used as received.

Impedance spectra were measured in the frequency range from 100 kHz to 0.1 Hz at varying potentials, which were scanned from positive to negative values and back (typically between 1.0 V to -0.7 V vs. Ag/AgCl in 0.5 M KCl, pH 2.5). The counter electrode was a platinum mesh. Impedance spectra were evaluated using Zview (Scribner) software.

Photoelectrochemical measurements were performed in an Ar-saturated 0.1 M Na_2SO_4 (pH 10) solution. The counter electrode was a platinum rod and the reference electrode was Ag/AgCl (sat. KCl). The photoelectrochemical cell was placed in a dark room and controlled by a potentiostat (Autolab PGstat 101, Metrohm with NOVA software). The working electrode was illuminated through fused silica optical window by a Hg lamp (Oriel); the spectral range was 320-380 nm, defined by optical filters.

3. RESULTS AND DISCUSSION

3.1. Structural and electrical properties

Table 1 summarizes the used preparative conditions and the measured values of sheet resistance (R_{sheet}), resistivity (ρ) and layer thickness. Raman spectra (Figure S2, Supporting Info) show broad bands typical of amorphous/highly disordered titanium oxide corresponding to high resistivity values of about 10 $\Omega \cdot cm$. Five distinct peaks at about 144, 197, 399, 519, 639 cm^{-1}, related to the Raman modes of anatase [30], are found in all heat-treated films, regardless of the annealing atmosphere. The effect of the deposition atmosphere pressure on the crystalline lattice parameters and vibrational frequencies has been discussed in [28,29]. It was assessed that the

structure, electronic and optical properties depend on the material defect chemistry in a non-trivial way.

The specific resistances, ρ of our films (Table 1) are comparable or better than the literature values for degenerately doped titania [22–24]. A Ta-free TiO_2 layer was prepared as a reference sample. The resistivity ($1.16 \cdot 10^{-2}$ $\Omega \cdot$cm) and the sheet resistance (R_{sheet}, 800 $\Omega/\square$ for a 150 nm thick film) of the Ta-free layer (Ta0) are considerably higher than those for FTO ($\sim 7 \cdot 10^{-4}$ $\Omega \cdot$cm, 13.4 $\Omega/\square$).

As discussed in the Introduction, carrier concentration depends on Ta content but is also strongly influenced by oxygen pressure during deposition, so that the optimal deposition pressure exists for the given Ta nominal content, at which the carrier concentration is maximized [29]. Upon doping with Ta a significant decrease of resistivity and R_{sheet} was obtained for samples prepared with an optimal deposition pressure of oxygen (≈ 1 Pa) and a post-deposition annealing in vacuum (sample Ta5a), as discussed in [27,29]. The 4-point electrical measurements show a metal-like behavior with a resistivity increase as a function of temperature [27]. Doping at deposition pressure of 2 Pa (Ta5b) resulted in a significant increase in the resistivity. The lowest value of resistivity was obtained for the Ta5a film with 5% of Ta deposited at 1 Pa ($\rho = 6.77 \cdot 10^{-4}$ $\Omega \cdot$cm, $R_{sheet} = 45$ $\Omega/\square$ for the 150 nm thickness) while either change of the Ta content to 1% or to 10% of Ta (samples Ta1 and Ta10, respectively, deposited at the optimal pressure conditions) resulted in the increase of resistivity and sheet resistance (Table 1). As expected, the sheet resistance proportionally decreased with increasing layer thickness from 150 nm to 500 nm (Ta5c and Ta5d, respectively).

Our best value of R_{sheet} (11.4 $\Omega/\square$) for a 500-nm thick TiO_2 (5% Ta, Ta5d) is comparable or even better than that of the used commercial FTO of similar layer thickness. This is promising in view of the prospective use of our doped titania films in the barrier-free, homo-junction DSCs. However, thermal treatment in air at 550ºC caused a strong increase of resistivity (samples Ta0-air and Ta5-air). This problem, which seems to be common to doped titania [23,25] as well as to ITO [5], presents a challenge for the fabrication of DSC photoanode, because the thermal annealing is a standard procedure in the preparation of mesoporous layers TiO_2 for dye-anchoring [1,2,31]. Obviously, the use of ultra-fast annealing procedures [27], low-temperature growth of mesoporous titania and/or the application of protective tunneling layers

6

(Al$_2$O$_3$ or ZrO$_2$) [20] for vacuum annealing need to be considered for future optimization of the manufacturing conditions towards 'all-titania' photoanodes.

The optical transparency of Ta-doped TiO$_2$ films also depends on the synthesis/annealing conditions as discussed in [27,28]. Typically, 150 nm thick undoped and Ta-doped TiO$_2$ films deposited at the optimal conditions and annealed in vacuum are characterized by an average transparency in the visible range (400-700 nm wavelengths) around 80%, and we thus focused our electrochemical investigation on the films with this thickness. The transmittance is mainly limited by reflectance (between ~10-25% in the visible range), and dominated by interference fringes depending on layer thickness, while the visible-light absorbance remains as low as ~5%. Increasing the film thickness improves the sheet resistance (Table 1) but lowers the optical transparency (by about 6% for a 290 nm thick layer).

3.2 Electrochemical behavior: cyclic voltammetry

Our layers were tested by cyclic voltammetry with Fe(CN)$_6^{3-/4-}$, Ru(bpy)$_3^{2+}$ and dimethylviologen (MV^{2+}) as model pH-independent redox probes with simple one-electron-transfer reaction. The redox potential of Fe(CN)$_6^{3-/4-}$ (0.24 V vs. Ag/AgCl) is sufficiently positive to the flatband potential (φ_{FB}) of TiO$_2$ (anatase) at all practically accessible pH values in aqueous media [10,32]:

$$\varphi_{FB} = -0.36 - 0.059 \cdot pH \text{ (V vs. Ag/AgCl)} \tag{1}$$

Figure 1 shows cyclic voltammograms of three TiO$_2$ films of the same thickness (150 nm) Ta5a, Ta5b and Ta0 in an aqueous electrolyte solution containing Fe(CN)$_6^{3-/4-}$. The films Ta5a and Ta5b have the same Ta content (5%) but were prepared at different deposition pressures of oxygen (1 and 2 Pa, respectively) Ta0 is a pure TiO$_2$ film. Ta doping and deposition pressure strongly influence the shape of voltammograms. The Ta-doped TiO$_2$ film deposited at 1 Pa (Ta5a) behaves almost like FTO. This film exhibits quasi-metallic nature, no rectifying effect (well-known for ordinary semiconducting titania) [8,9] is observed. On the other hand the voltammograms of pure TiO$_2$ film or Ta-doped TiO$_2$ film deposited at 2 Pa show irreversible electrochemical behavior characterized by larger peak-to-peak splitting.

Nevertheless, even the Ta-free (Ta0) electrode shows the anodic wave of ferrocyanide oxidation (Fig. 1, curve c). This is interesting in view of its total absence in compact FTO-supported TiO_2 films made earlier by sol-gel (with donor density, N_D = (3-5)·10^{20} cm^{-3}) [9], by spray-pyrolysis, ALD or electrodeposition (with donor density, N_D = (1-7)·10^{20} cm^{-3}) [8]. Though the comparable intrinsic doping of our Ta0 sample ($\approx 10^{20}$ cm^{-3} see below) and the previously reported TiO_2 layers [8,9] we observe this qualitative difference for our Ta0 layer. We can speculate that inhomogeneous doping (with metallic islands in semiconducting matrix) could occur during the PLD-process, but we leave this question open at this stage of our research.

Figure 2 shows the influence of scan rate on the cyclic voltammograms of 5%Ta-doped TiO_2 film deposited at O_2 pressure of 1 Pa (Ta5d). The film has a layer thickness of 500 nm, i.e. comparable to that of our reference FTO. The plot confirms the quasi-reversible electrochemistry of the $Fe(CN)_6^{3-/4-}$ couple with the peak-to-peak splitting (ΔE_{pp}) of 80-110 mV for the scan rates from 50 to 200 mV/s, respectively. The FTO reference provided at the same conditions ΔE_{pp} from 66 to 82 mV (Fig. S3, Supporting Info). Hence, the charge-transfer rate constant is only slightly smaller at the Ta-doped TiO_2 referenced to that on FTO. Figures 1, 2 and S3 further illustrate the effect of Ta content (1-10%) on the ΔE_{pp}. The charge-transfer is markedly slower for the lowest Ta doping (1%), but the films with higher Ta doping (5 and 10%) behave similarly. There is only marginal effect of the film thickness on the electrochemical reversibility of the otherwise identical layers (150-500 nm, samples Ta5a, Ta5c and Ta5d). On the other hand, the air-annealed samples (Ta5-air, Ta0-air) show no electrochemical activity for this redox couple, which is interrelated with their insulating nature (Table 1).

The cyclic voltammograms in pure supporting electrolyte solution (Fig. 3) exhibit a standard shape with reversible charging/discharging of chemical capacitance (C_μ) at potentials below the flatband potential. This is consistent with the filling/emptying of the exponentially growing density of states near the CB edge [9,33–35]. Sometimes, a small pre-peak was reported at potentials slightly positive to φ_{FB} which is assignable to the trap states (surface states) below the CB [33,36,37]. Jankulovska et al. [35] correlated the occurrence of this pre-peak with the structural perfection of the respective TiO_2 electrodes: it was missing on well-defined surfaces, but was omnipresent in the voltammograms of mesoporous nanocrystalline electrodes, both in aqueous [33] and non-aqueous media [36]. The absence of the electrochemically detectable

surface states in our Ta-doped layers reminds the same behavior of dense TiO$_2$ layers made by sol-gel [9], electrodeposition [8] or ALD [8] and is considered a proof of their structural quality.

Eq. (1) predicts φ_{FB} = -0.51 V vs. Ag/AgCl for pure anatase single-crystal in this electrolyte solution (the experimental values was -0.54 V vs. Ag/AgCl for Ta0, see Section 3.2). Fig. 3A (left chart), indeed confirms that the onset of the charging of CB states is located near this predicted φ_{FB} position. A closer inspection of the voltammogram in Fig. 3A reveals another peculiar feature, which is specific for our Ta-doped electrodes only. While in the ordinary semiconducting TiO$_2$ electrodes, the voltammetric current rapidly drops to almost zero at potentials positive to φ_{FB} [8,9,33,35,36,38], our Ta-doped layers show a significant voltammetric current (i_c) even at potentials between ca. 0 to 1 V vs. Ag/AgCl. Its capacitive nature is confirmed by the scan-rate (v) dependence:

$$C = i_c/v \tag{2}$$

where C is the total interfacial capacitance. Inset in Fig. 3A shows an example plot (according to Eq. 2 at 0.5 V vs. Ag/AgCl) from which $C \approx 35\ \mu F/cm^2$. The fact that the current does not drop to zero at positive potentials can be attributed to high concentration of electron-donor sites provided by Ta doping. However, the voltammogram is not perfectly rectangular, as one would expect for purely double-layer charging on metallic electrodes. In general, the total capacitance of the TiO$_2$/solution interface has three main contributions: the double-layer (Helmholtz) capacitance (C_H), the space charge capacitance (C_{SC}) formed at the semiconductor surface and the chemical capacitance (C_μ) which is interrelated with proton insertion into TiO$_2$ at sufficiently negative potentials ($\varphi < \varphi_{FB}$) [8,9,37−40]:

$$TiO_2 + e^- + H^+ \rightarrow TiOOH \tag{3}$$

The total capacitance is a parallel combination of C_{SC} and C_μ, while C_H is connected in series to the former two [41,42]:

$$\frac{1}{C} = \frac{1}{C_{SC} + C_\mu} + \frac{1}{C_H} \tag{4}$$

C_μ appears at potentials lower than φ_{FB}, so its contribution can be neglected at $E > 0$ V vs. Ag/AgCl. On the other hand, at sufficiently negative potentials (in the hydrogen insertion/evolution region, cf. Eq. 3) the C_μ becomes significantly larger than C_H, so that $C \to C_H$ [40,43]. Within these approximations, the capacitance $C \approx 35$ µF/cm^2 estimated from the current, i_c at 0.5 V vs. Ag/AgCl stems from the series combination of C_{SC} and C_H. For evaluation of sole double-layer capacitance, we need to use the electrochemical impedance spectroscopy [40] (see below).

Some changes arise in the voltammogram in pure supporting electrolyte, if the electrode passed long-term (hours) polarization at potentials between 1 and -0.8 V. This is documented in Fig. 3B (right chart). The changes in cyclic voltammogram upon this treatment are attributed to the electrochemical doping by H$^+$ insertion [8,37,38]. As in the case of dense layer made by sol-gel [38], electrodeposition [8] or ALD [8], we observe an enhanced cathodic current which is specific for the H-doping. The H-doping is more stable for compact films [8,38] as compared to porous films composed from individual nanoparticles, the latter are known to reverse back to the H-undoped state within ca. hours of aging [37].

Despite that fact that our Ta-TiO₂ electrodes show metal-like behavior (mimicking FTO) in contact with Fe(CN)$_6^{3-/4-}$, a strikingly different response is observed for a redox probe with more positive redox potential. Figure 4 shows that the cyclic voltammogram of Ru(bpy)$_3^{3+/2+}$ redox couple is fully blocked at the Ta-TiO₂ electrodes. This would indicate that Ta-TiO₂ is not entirely 'metal-like' but forms a rectifying interface for highly positive redox probes. Though we cannot demonstrate the rectifying function for the reduction of Ru(bpy)$_3^{3+}$ below the φ_{FB} (due to the unavailability of the Ru(III) species) this finding is qualitatively supported by our observation of significant UV-photocurrents for our Ta-doped titania, *vide infra..*

To address the difference between Fe(CN)$_6^{3-/4-}$ and Ru(bpy)$_3^{3+/2+}$, we recall the fact that thin space charge region (depletion layer), is known to exist even on degenerate semiconductors like on FTO [8,44–47]. Its thickness, L_D scales with the dielectric constant ε_r, the donor density N_D and the applied voltage φ:

$$L_D = \left(\frac{2\varepsilon_0 \varepsilon_r}{eN_D} \right)^{1/2} \left(\phi - \phi_{FB} - \frac{kT}{e} \right)^{1/2} \tag{5}$$

(e is the electron charge, ε_0 is the permittivity of free space, k is the Boltzmann's constant and T is the temperature). For a bare FTO electrode the dielectric constant ($\varepsilon_r \approx 9$) [45] is much smaller than that of TiO$_2$ ($\varepsilon_r \approx 55$) [8,9] and the donor density of FTO ($N_D = 6.5 \cdot 10^{21}$ cm^{-3}) [8] is similar or larger than the values found for our Ta-TiO$_2$ layers (see Section 3.3 and Table 2 below). Hence, we propose that for highly positive redox couples like Ru(bpy)$_3^{3+/2+}$ (with high φ) and the assumption of Fermi level pining, the barrier introduced by larger space-charge field effectively blocks the anodic charge-transfer. Eq. (5) provides an estimate of $L_D \approx 4.2$ nm in a model calculation for $N_D \approx 10^{21}$ cm^{-3}, $\varphi_{FB} = -0.6$ V (Table 2) and the applied potential for the Ru(bpy)$_3^{2+}$ oxidation, $\varphi \approx 1.1$ V vs. Ag/AgCl (Fig. 4). This space-charge barrier effectively blocks the electron tunneling from/to the semiconductor to/from the electrolyte. On the other hand, the same model calculation for FTO provides $L_D \approx 0.5$ nm, which is considerably thinner, and the electron transfer is feasible in both directions. In addition to this interpretation, we can also assume that attractive interaction between the positively charged titania surface and negatively charged Fe(CN)$_6^{3-/4-}$ facilitates the charge transfer (and contrariwise for Ru(bpy)$_3^{3+/2+}$).

To further illustrate this discussion, we selected another positively charged model redox probe, but with smaller redox potential, i.e. dimethylviologen, MV$^{2+/+}$. Figure S4 (Supporting Info) shows that FTO expectedly behaves like metallic electrode, i.e. the reduction/oxidation peaks of MV$^{2+/+}$ do not move with pH. With respect to Eq. (1), the redox potential of MV$^{2+/+}$ (-0.65 V vs. Ag/AgCl) is close to φ_{FB} of TiO$_2$ in slightly acidic medium (pH 5.8) but positive to φ_{FB} in alkaline medium (pH 11.3). Consequently, the anodic wave of MV$^+$ oxidation is normally not seen in alkaline medium for 'ordinary' semiconducting TiO$_2$, because it is in a depletion regime at these conditions [8]. However, the MV$^{2+/+}$ redox couple is active at the Ta-doped TiO$_2$ surface like on metal due to smaller φ and thus negligible barrier of the space-charge field (Eq. 5). Both anodic and cathodic current peaks are present, though the currents are smaller than those for FTO and there is slightly enhanced irreversibility in alkaline medium.

3.3 Electrochemical impedance spectroscopy

Electrochemical impedance spectroscopy (EIS) is used to explore the conduction-band position in n-doped semiconductor electrodes through the Mott-Schottky plots. Figure 5 shows a typical plot of our Ta-TiO$_2$ electrode (other plots are included in the Supporting Info, Fig. S5). The

experimental EIS spectra (see Fig. S6 in Supporting Info) were fitted to the equivalent circuit shown in Fig. S7 (Supporting Info). This provides the serial ohmic resistance of electrodes, electrical contacts and electrolyte solution (Rs), and the charge-transfer resistance, R_{CT}. The impedance of the CPE equals:

$$Z_{CPE} = B(i\omega)^{-\beta} \tag{6}$$

where ω is the EIS frequency and B, β are the frequency-independent parameters of the CPE ($0 \leq \beta \leq 1$). The value of capacitance, C is obtained from Z_{CPE} as follows:

$$C = \frac{(R_{CT} \cdot B)^{1/\beta}}{R_{CT}} \tag{7}$$

An obvious advantage of this evaluation protocol is that it removes the virtual 'frequency dispersion' of Mott-Schottky plots [8,9,32]. The Mott-Schottky equation used to analyze the data is [44]:

$$\frac{1}{C^2} = \left(\frac{2}{e\varepsilon_0\varepsilon_r N_D}\right)\left(\phi - \phi_{FB} - \frac{kT}{e}\right) + \frac{1}{C_H^2} \tag{8}$$

The double-layer contribution (C_H) does not influence the slope of Mott-Schottky plots, but causes a negative displacement of the flatband potential from the potential-axis intercept of the experimental plot by $\Delta\varphi_{FB}$:

$$\Delta\varphi_{FB} = \frac{e\varepsilon_r\varepsilon_0 N_D}{2C_H^2} \tag{9}$$

The correction term can further include the contributions from diffuse layer and from a thin dielectric layer, which can be present at the titania surfaces [48]. The value of C_H can be estimated from the total capacitance at the negative potential limit (cf. Eq. 4 and discussion thereof) [40]. Inset in Fig. 5 shows this dependence; additional data are presented in Fig. S5 (Supporting info). Except for the sample Ta10, there are no signs of the capacitance limit ($C \rightarrow C_H$) even at the lowest applied potential. Hence, this analysis provides only the lower estimate of C_H of ca. 130-200 µF/cm^2 in all our samples. This value is smaller than that found for

compact TiO$_2$ film made by anodization of Ti (C$_H$ = 470 μF/cm^2) [40] but larger than some other literature values reported for oxidic electrodes (10-50 μF/cm^2) [44,49,50]. This spread of literature data is obviously caused by the fact that the experimental capacitances are normalized to the projected (cross-sectional) electrode areas, i.e. they primarily reflect the electrochemically accessible surface area of the particular electrode, rather than the standard double-layer capacitance of a flat oxide surface [40]. Furthermore, we should note that the double layer formed at deeply negative potentials is inherently different from that formed in depletion regime. In spite of these reservations, the correction term (Eq. 9) is very small, between 0.02 to 0.0004 V for all our samples, if we use ε$_r$ ≈ 55 (as for pure anatase) [8,9] and N_D from the Hall measurements (Table 2).

The found values of φ_{FB} (Table 1) for undoped (Ta0) are close to the literature value for single-crystal anatase (-0.51 V vs. Ag/AgCl, see Eq. 1). This finding is not trivial, as the φ$_{FB}$ is known to vary for pure anatase films having nanocrystalline morphology [8,9,38]. The Ta-doping causes zero or very small downshift of φ_{FB} (Table 1). Our finding matches the work of Ghosh et al. [18] who reported no significant differences between the φ$_{FB}$ values of pure and Ta-doped anatase in aprotic electrolyte solution. In contrast, Liu et al. [17] reported ca. 0.2 V upshift of the φ$_{FB}$ for Ta-doped TiO$_2$ as referenced to pure TiO$_2$. The donor concentrations, N_D found from EIS are reasonably close to values determined by Hall measurements (Table 2), but in most cases the Hall measurements provide smaller N_D values. The same difference of Hall/EIS was observed in SnO$_2$ films [12]. It was ascribed to several factors, the most plausible one (also for our Ta-TiO$_2$ films) seems to be the fact that Hall-effect is occurring in the bulk, whereas EIS is addressing solely the thin (space-charge) layer on the surface.

3.4. UV-photoelectrochemistry

The occurrence of anodic photocurrent of water oxidation is a well-known effect upon UV (band-gap) excitation of semiconducting titania electrodes [10,32,51], but it should be absent on metallic electrodes, where the exciton is rapidly quenched due to absence of space-charge field. However, we observed here surprisingly high photocurrents even on metal-like, Ta-doped titania. Figure 6 shows the influence of Ta-doping on the photoelectrochemical behavior of TiO$_2$

films under UV light. The largest photocurrent density was expectedly found for our Ta-free sample (Ta0), which behaves nearly like an ideal (single-crystal) anatase [10,32].

The overall photocurrent density gradually decreases with increasing Ta content and the shape of the current/potential curves is different too (Fig. 6). Nevertheless, the photocurrents at large band bending (the applied anodic potential) are still of the order of 10 $\mu A/cm^2$ at the employed UV-light intensity even for high Ta-doping. The trend of decreasing photocurrent with Ta-concentration follows the gradual enhancement of the optical band gap (from 3.31 to 3.44 eV) [28]. It is also reminiscent of the photocurrent drop of Ta-doped TiO_2 nanotubes (0.1-0.4% Ta) where it was interpreted in terms of defects acting as recombination centers [21]. The potential of the onset of photocurrent is more positive than the flatband potential, $\varphi_{FB} \approx$ -1 V vs. Ag/AgCl which is expected at pH 10 (Eq. 1 and Table 2). Hence, the photoelectrochemical reactions at our degenerate semiconductors require a driving force of enhanced band-bending (ca. 0.3-0.5 V).

Figure 7 compares the current densities of the reference FTO substrate and two 5% Ta-doped films with the same layer thickness (150 nm) but prepared at different oxygen deposition pressure (1 and 2 Pa). Larger photocurrents were obtained for the sample Ta5b (2 Pa O_2) and there is a relation with the electrochemical behavior (Fig.1, Table 2), i.e. the decreased charge-transfer reversibility of Ta5b is accompanied by the increased photocurrent. The onset of photocurrent occurs for Ta5b at more negative potentials, consistent with its more negative φ_{FB} (Table 2). The dependence of photocurrent on layer thickness of 5% Ta-doped TiO_2 films is not monotonic, but the largest photocurrents are observed for the thinnest film (150 nm; Figure S8a Supporting Info). The photocurrents at the reference FTO are very low, but not zero at larger potentials.

The photoelectrochemical activity is quantified by a photocurrent value at certain arbitrarily selected applied potential providing sufficient band bending (1.05 V vs. Ag/AgCl). Table 2 collects the relevant data. In general, the occurrence of photocurrent on Ta-doped TiO_2 is surprising in view of its quasi-metallic nature. This finding illustrates again the unexpected semiconductor-like behavior for model redox probe with high redox potential (cf. Fig. 4). The air-annealed samples (despite their very high resistances) show UV photocurrent only if Ta is present (Fig. S8b, Supporting Info).

3.5. Li-insertion electrochemistry

Cyclic voltammetry of Li-insertion is a sensitive method for analyzing details of phase composition and other parameters of titania electrodes [10,32,52,53]. The Li$^+$ insertion reaction is formally analogous to the proton insertion (cf. Eqs 4 and 10):

$$TiO_2 + x(Li^+ + e^-) \rightarrow Li_xTiO_2 \tag{10}$$

where $x \approx 0.5$ is usually found for anatase.

The integrated anodic charges (Fig. 8; shaded areas at the corresponding voltammograms) equal: 3.3, 6.7 and 12.5 mC/cm^2 for the samples Ta5a, Ta5b and Ta0, respectively, as determined at the scan rate of 0.1 mV/s. The corresponding cathodic charges equal -7.0, -11.7 and -18.3 mC/cm^2 for the same samples. Hence, there is significant misbalance of cathodic (Li-insertion) vs. anodic (Li-extraction) charges. Analogous effect was observed on voltammograms of macroscopic single crystal anatase electrode, where the cathodic and anodic charges were -54.0 mC/cm^2 and 26.4 mC/cm^2, respectively, at the scan rate of 0.1 mV/s [32]. On the other hand, mesoporous anatase electrodes usually exhibit well balanced insertion/extraction charges [52–54], yet there is also strong contribution of capacitive charging at nanocrystalline TiO$_2$ [52]. The striking difference between compact anatase electrodes (both single crystal and polycrystalline) and mesoporous ones is attributed to solid-state diffusion effects.

More specifically, Li$^+$ ions which have been inserted during the initial cathodic scan into the subsurface region of compact titania solid continue diffusing into the bulk in the subsequent extraction step, too. These deeply penetrating Li$^+$ ions are not recovered in the reverse (anodic) scan at the time scale of cyclic voltammogram. The voltammogram of our Ta-free sample (Ta0) shows a factor of 2-3 smaller Li$^+$-loading compared to single crystal electrode, which is attributed to slowdown of Li-transport at grain boundaries in polycrystalline films. (It manifests itself also by orders-of-magnitude smaller diffusion coefficient of Li in polycrystalline electrodes [53] compared that in single crystal electrode [32]).

Though we cannot rule out that the whole film is homogeneously loaded with lithium at smaller insertion coefficient ($x < 0.5$ cf. Eq. 10) the observed charge-misbalance speaks against this assumption. An alternative limiting model is that the Li-rich subsurface layer has the ultimate

composition ($Li_{0.5}TiO_2$) and the bulk film is free from Li at the initial stages of potential scanning. In this approximation, the found cathodic charges translate into the thickness of the $Li_{0.5}TiO_2$ sub-surface film of 17, 51 and 77 nm for the samples Ta5a, Ta5b and Ta0, respectively. The metallic conductivity is clearly distinguished on the Li-extraction (anodic) peak, which extends towards potentials as large as 3 V vs. Li/Li^+. In contrast, 'truly' semiconducting (Ta-free) anatase shows negligible voltammetric currents at potentials positive to ca. 2.3 V vs. Li/Li^+, when the electrode is in strong depletion and virtually insulating [52–54]. The Li-storage activity of the Ta-doped samples is further surveyed in Fig. S9 (Supporting Info).

Figures 8 and S9 confirm that the Li-insertion activity decreases with the concentration of Ta; in addition to secondary effects of the layer thickness (samples Ta5a, Ta5c, Ta5d) and preparative details (samples Ta5a, Ta5b). The monotonic drop of Li-insertion activity with Ta-concentration in the series of comparable samples, i.e. Ta0, Ta1, Ta5a and Ta 10, is significant. We propose that the Ta^{5+} cations, which occupy Ti^{4+} sites in the anatase lattice [26] provide repulsive charge impeding the Li^+-insertion. Quite interesting is the negligible activity of the air-annealed Ta-free sample as compared to the same sample with 5 % Ta. This trend is qualitatively reproduced also by the occurrence of the UV-photocurrent at the Ta5-air sample (Figure S8). In spite of the fact that that both the air-annealed samples have very high resistivity, solely the Ta-containing sample (Ta5-air) exhibits some electrochemical activity for these two principally different charge-transfer processes.

4. CONCLUSIONS

Highly conducting ($\rho \approx 10^{-4}$ $\Omega \cdot cm$, $R_{sheet} \approx$ 11 Ω/sq) Ta-doped TiO_2 (anatase) thin films were deposited by PLD on ordinary soda-lime glass substrate. Quasi-reversible voltammograms of $Fe(CN)_6^{3-/4-}$ and dimethylviologen MV^{2+} redox couples are observed on these films, mimicking the electrochemical activity of FTO. However, the analogy with FTO is not absolute, because the Ta-doped TiO_2 films are idle for the $Ru(bpy)_3^{2+}$ oxidation. This is attributed to a larger space-charge barrier on Ta-doped TiO_2 for redox couples with highly positive electrochemical potentials.

Our Ta-doped TiO_2 films exhibit both the metal-like capacitive charging and the semiconductor-like chemical capacitance in pure supporting electrolyte solutions. These two effects manifest

themselves in cyclic voltammograms at potentials positive or negative, respectively to the flatband potential. Its value is near that of the pure anatase single-crystal electrode, and almost independent of Ta-doping, as determined by electrochemical impedance spectroscopy from Mott-Schottky plots.

All our TiO_2 layers, both pristine and Ta-doped, exhibit photoelectrochemical activity with photocurrents of the order of 10-100 $\mu A/cm^2$ upon irradiation with UV light (wavelength 320-380 nm; intensity 2.5 mW/cm^2). The photocurrents decrease proportionally to the increase of Ta-content. The photocurrent onset in linear-sweep voltammetric scans occurs at potentials which are positive to the φ_{FB} by ca. 0.3 to 0.5 V. The UV-photocurrent is another signature of the dual performance (semiconductor/metal) of our electrodes.

All our TiO_2 layers, both pristine and Ta-doped, are active for electrochemical Li-insertion. As in the case of UV-photocurrent, the accessible Li-insertion charge decreases proportionally with the increasing Ta-content. This is attributed to the repulsive charge of Ta^{5+} cations occurring at the Ti^{4+} sites in the anatase lattice. The Li-extraction peak in cyclic voltammograms confirms the quasi-metallic nature of Ta-doped TiO_2: there is no cut of anodic current, which normally occurs on semiconducting TiO_2 in depletion regime.
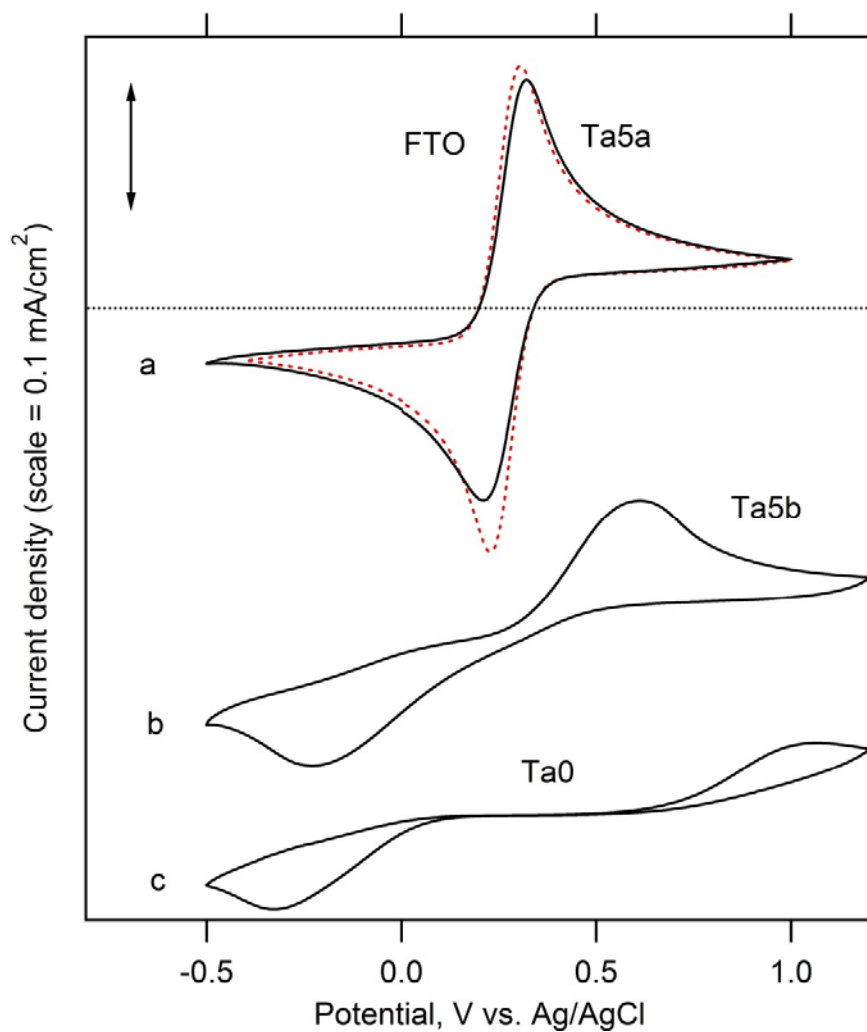
Figure 1: Cyclic voltammograms of (a) FTO (red dashed curve) and Ta5a (black curve); (b) Ta5b and (c) Ta0 samples; scan rate 50 mV/s. The electrolyte solution was 0.5 mM $K_4[Fe(CN)]_6$ + 0.5 mM $K_3[Fe(CN)]_6$ in aqueous 0.5 M KCl, pH 2.5. Voltammograms (b) and (c) are offset for clarity, but the current scales are identical. Dashed horizontal line is the zero-current level for the voltammograms (a).
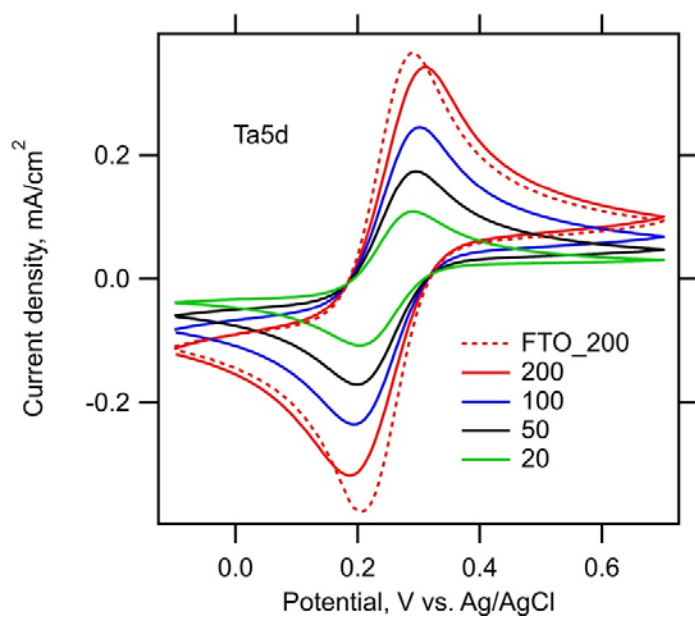
Figure 2: Cyclic voltammograms of the Ta5d sample (5%-Ta, 500 nm layer thickness) at scan rates 50, 100 and 200 mV/s. A reference voltammogram for FTO electrode (at 200 mV/s) is shown by dashed line for comparison. The electrolyte solution was 0.5 mM $K_4[Fe(CN)]_6$ + 0.5 mM $K_3[Fe(CN)]_6$ in aqueous 0.5 M KCl, pH 2.5.
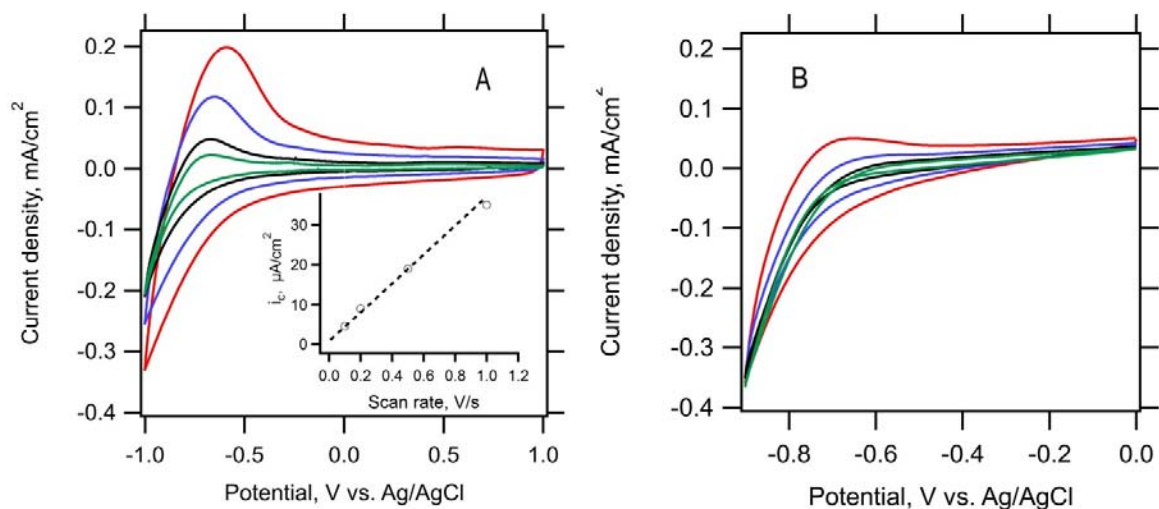
Figure 3: Cyclic voltammograms of Ta5b sample at scan rates 50, 100, 200, 500 and 1000 mV/s. The electrolyte solution was aqueous 0.5 M KCl, pH 2.5. Chart (A) shows voltammogram of a fresh electrode. Chart (B) shows the voltammogram of the same electrode after passing three subsequent measurements of EIS between 1 and -0.5 V vs. Ag/AgCl. Inset in the chart (A) shows the capacitive current, i_{cap} (measured at 0.5 V vs. Ag/AgCl) as a function of the scan rate.
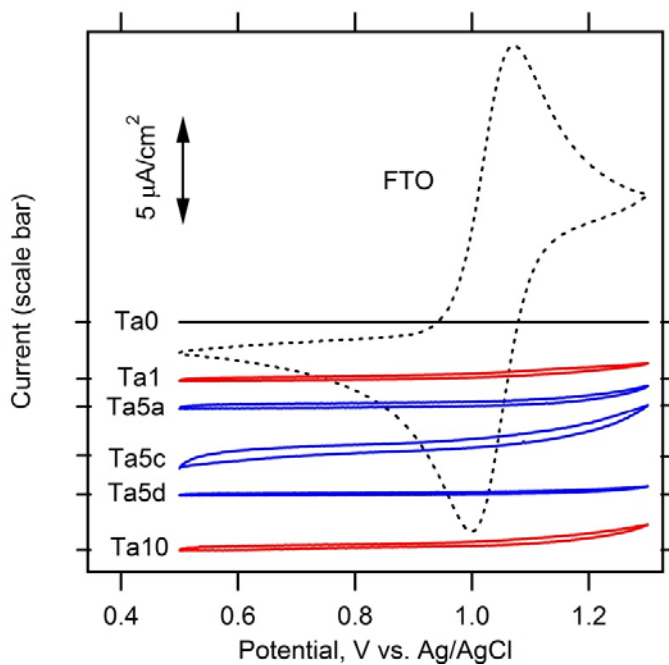
Figure 4: Cyclic voltammograms of a FTO electrode (dashed line) and the other sample electrodes (full lines). Scan rate 50 mV/s. The electrolyte solution was 0.1 mM $Ru(bpy)_3Cl_2$ in aqueous 0.5 M KCl, pH 2.5. Curves for Ta1-Ta10 are offset for clarity, but the intensity scale is identical for all voltammograms; ticks on vertical axes define the zero-current levels.
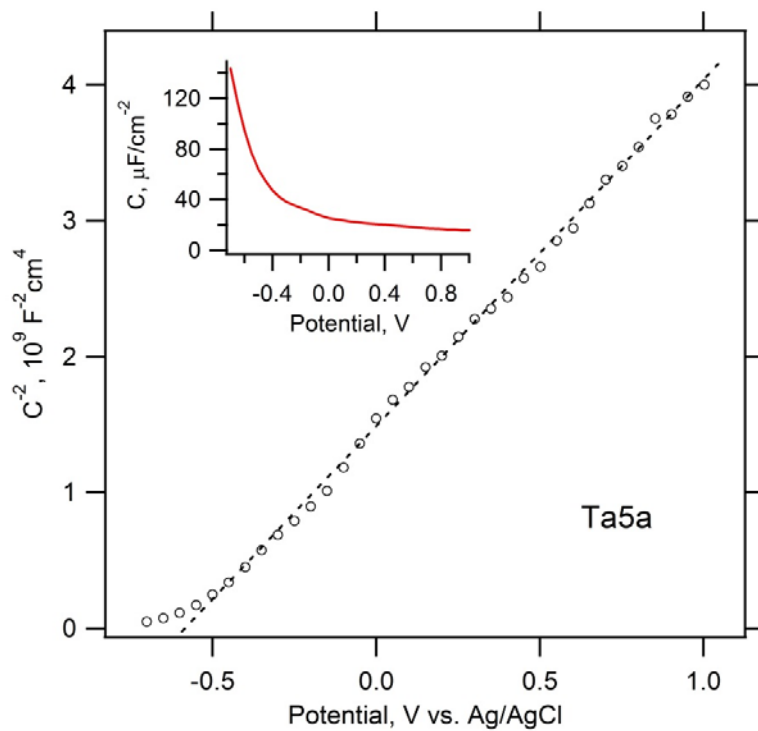
Figure 5: Mott-Schottky plot of the Ta5a electrode. Electrolyte solution: 0.5 M KCl, pH 2.5. Inset shows the potential dependence of capacitance.
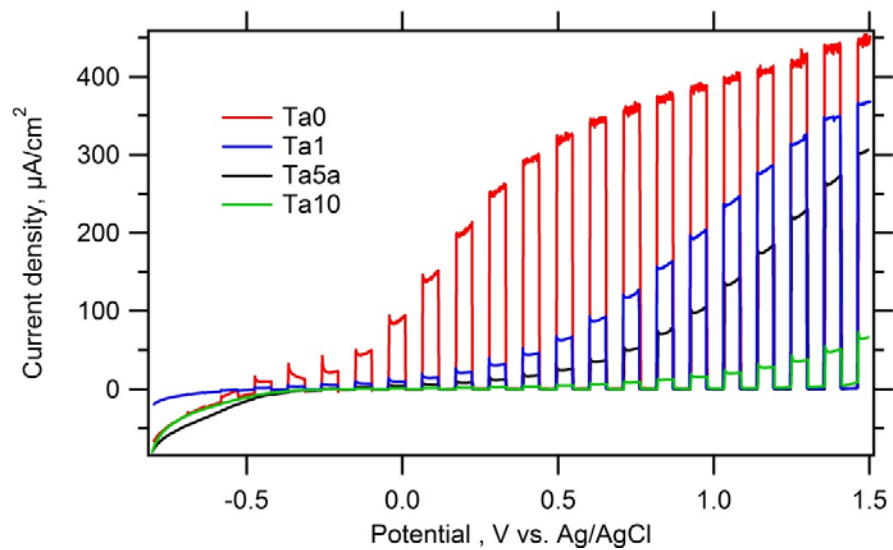
Figure 6: Linear sweep voltammetry (scan rate 5 mV/s) under chopped UV light (Hg lamp 320-380 nm) intensity 2.5 mW/cm^2 for samples with different amount of Ta. The electrolyte solution 0.1 M Na$_2$SO$_4$ (pH 10), dark/light intervals of 10 s. Layer thickness is 150 nm for all four films presented.
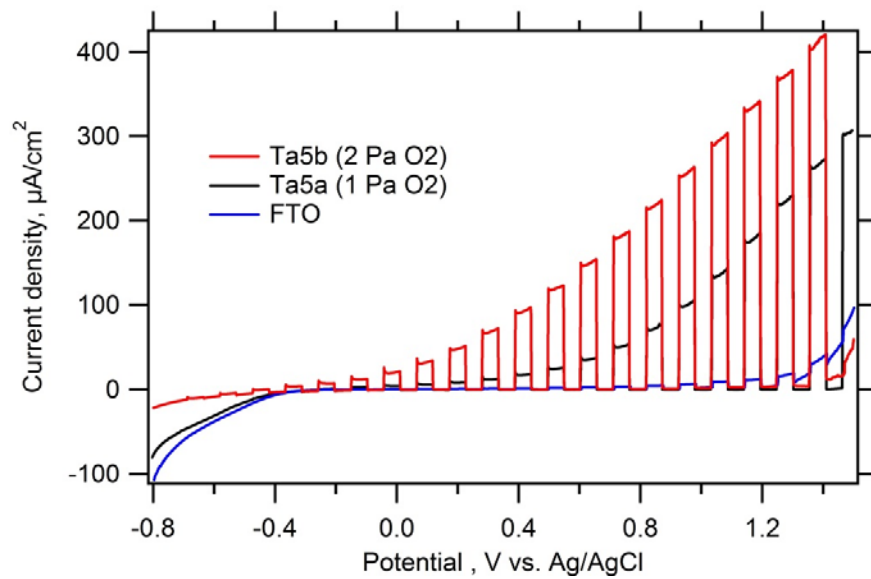
Figure 7: Linear sweep voltammetry (scan rate 5 mV/s) under chopped UV light (Hg lamp 320-380 nm) intensity 2.5 mW/cm^2. Two samples are compared with the same Ta content (5 %) and layer thickness (150 nm), but with different deposition pressure of O_2 (Table 1). Control experiment with pure FTO electrode is also presented. The electrolyte solution 0.1 M Na_2SO_4 (pH 10), dark/light intervals of 10 s.
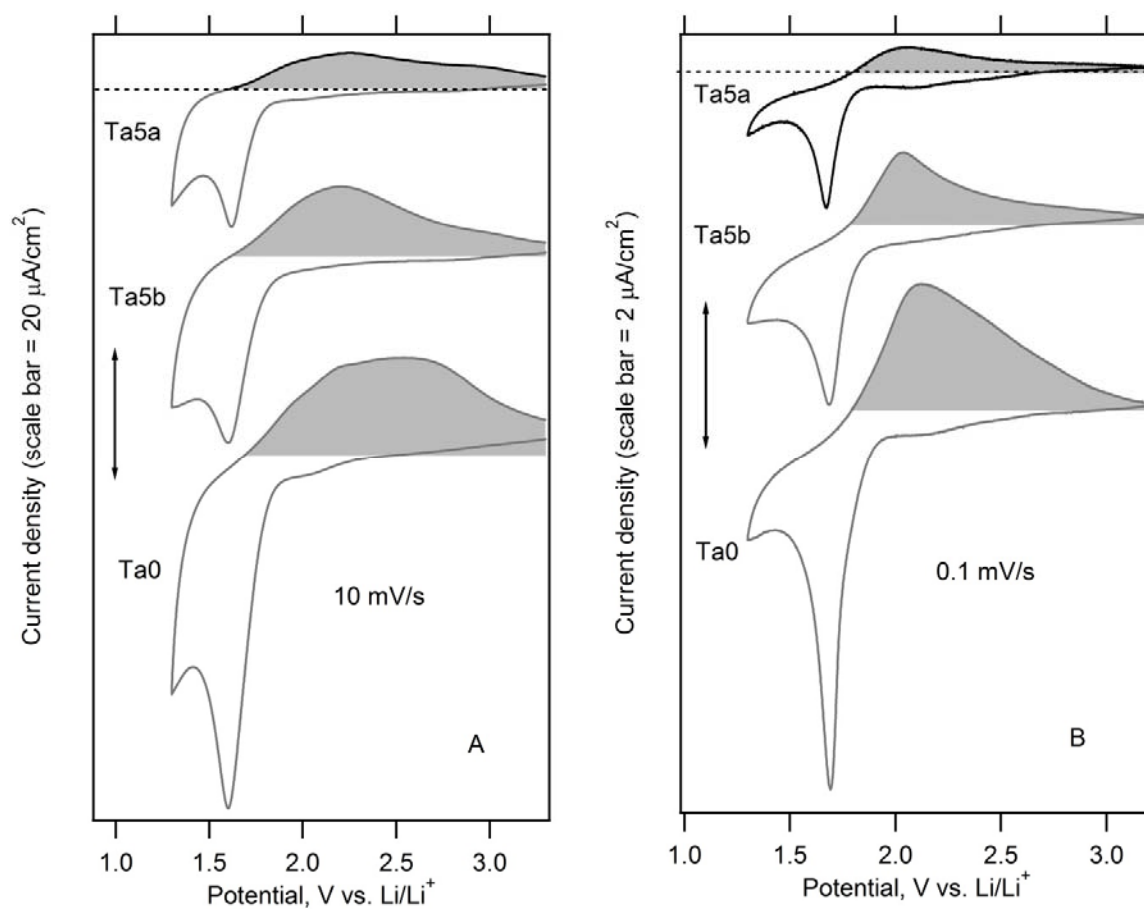
Figure 8: Cyclic voltammograms of the Ta5a, Ta5b and Ta0 samples in 1 M LiClO$_4$ + EC/DMC. Left chart (A): scan rate 10 mV/s; right chart (B) 0.1 mV/s. Shaded areas highlight the anodic (extraction) charge. Curves are offset for clarity but the intensity scale is identical for all voltammograms in the respective window. Dashed line is the zero current-level for the sample Ta5a.

Table 1: Deposition conditions (PLD) and basic properties of the used layers.

sample code	Ta (%)	deposition pressure (Pa)[a]	annealing atmosphere[b]	R_{sheet} ($\Omega/\square$)	resistivity, ρ ($\Omega \cdot cm$)	layer thickness (nm)
Ta0	0	1.4	vacuum	776	$1.16 * 10^{-2}$	150
Ta1	1	1	vacuum	120	$1.79 * 10^{-3}$	150
Ta5a	5	1	vacuum	45	$6.77 * 10^{-4}$	150
Ta5b	5	2	vacuum	5450	$8.18 * 10^{-2}$	150
Ta5c	5	1	vacuum	19	$5.57 * 10^{-4}$	290
Ta5d	5	1	vacuum	11.4	$5.72 * 10^{-4}$	500
Ta10	10	1.25	vacuum	65	$9.82 * 10^{-4}$	150
Ta5-air	5	1.25	air	not measurable	not measurable	150
Ta0-air	0	1.4	air	not measurable	not measurable	150
FTO (ref)	-	-	-	13.4	$6.72 * 10^{-4}$	500

[a] The used gas was O_2 in all cases.
[b] The temperature of annealing was 550 °C in all cases.

Table 2: Donor concentrations and electrochemical parameters.

sample code	donor density from Hall effect (cm^{-3})	donor density from EIS (cm^{-3})	flatband potential, φ_{FB} (V vs. Ag/AgCl)[b]	UV-photocurrent @1.05 V vs. Ag/AgCl ($\mu A/cm^2$)[c]
Ta0	$1.18 \cdot 10^{20}$	$1.6 \cdot 10^{20}$	-0.54	395
Ta1	$2.70 \cdot 10^{20}$	$6.0 \cdot 10^{21}$	-0.59	236
Ta5a	$7.99 \cdot 10^{20}$	$1.0 \cdot 10^{21}$	-0.59	133
Ta5b	$3.76 \cdot 10^{19}$	$6.8 \cdot 10^{20}$	-0.61	290
Ta5c	$8.61 \cdot 10^{20}$	$1.1 \cdot 10^{21}$	-0.55	83
Ta5d	$8.98 \cdot 10^{20}$	$7.9 \cdot 10^{20}$	-0.58	98
Ta10	$1.76 \cdot 10^{21}$	$1.5 \cdot 10^{21}$	-0.54	20
FTO (ref)	$3.77 \cdot 10^{20}$	[a]$6.5 \cdot 10^{21}$	[a]-0.30	6

[a] Data from Ref. [8]
[b]pH = 2.5
[c]pH = 10

References

[1] K. Kalyanasundaram, Dye Sensitized Solar Cells, CRC Press Taylor & Francis, Boca Raton, 2010.

[2] A. Hagfeldt, G. Boschloo, L. Sun, L. Kloo, H. Pettersson, Dye-Sensitized Solar Cells, Chem. Rev. 110 (2010) 6595-6663.

[3] N. Armaroli, V. Balzani, Solar Electricity and Solar Fuels: Status and Perspectives in the Context of the Energy Transition, Chem. Eur. J. 22 (2016) 32-57.

[4] L. Kavan, P. Liska, S.M. Zakeeruddin, M. Grätzel, Low-temperature Fabrication of Highly-Efficient, Optically-Transparent (FTO-free) Graphene Cathode for Co-Mediated Dye-Sensitized Solar Cells with Acetonitrile-free Electrolyte Solution, Electrochim. Acta 195 (2016) 34-42.

[5] S. Lee, J.H. Noh, S.T. Bae, I.S. Cho, J.Y. Kim, H. Shin, J.K. Lee, H.S. Jung, K.S. Hong, Indium-tin-oxide-based Transparent Conducting Layers for Highly Efficient Photovoltaic Devices, J. Phys. Chem. C 113 (2009) 7443-7447.

[6] H.J. Snaith, M. Grätzel, The Role of a "Schottky Barrier" at an Electron-collection Electrode in Solid-state Dye-sensitized Solar Cells, Adv. Mater. 18 (2006) 1910-1914.

[7] S. Lee, J.H. Noh, H.S. Han, D.K. Yim, D.H. Kim, J.K. Lee, J.Y. Kim, H.S. Jung, K.S. Hong, Nb-doped TiO2: A new Compact Layer Material for TiO2 Dye-sensitized Solar Cells, J. Phys. Chem. C 113 (2009) 6878-6882.

[8] L. Kavan, N. Tetreault, T. Moehl, M. Grätzel, Electrochemical Characterization of TiO2 Blocking Layers for Dye Sensitized Solar Cells, J. Phys. Chem. C 118 (2014) 16408-16418.

[9] L. Kavan, M. Zukalova, O. Vik, D. Havlicek, Sol-Gel Titanium Dioxide Blocking Layers for Dye-Sensitized Solar Cells: Electrochemical Characterization, Chemphyschem 15 (2014) 1056-1061.

[10] L. Kavan, Electrochemistry of Titanium Dioxide: Some Aspects and Highlights, Chem. Rec. 12 (2012) 131-142.

[11] H. Zhou, Q. Chen, G. Li, S. Luo, T.B. Song, H.S. Duan, Z. Hong, J. You, Y. Liu, Y. Yang, Interface Engineering of Highly Efficient Perovskite Solar Cells, Science 345 (2014) 542-546.

[12] L. Kavan, L. Steier, M. Grätzel, Ultrathin Buffer Layers of SnO2 by Atomic Layer Deposition: Perfect Blocking Function and Thermal Stability, J. Phys. Chem. C 121 (2017) 342-350.

[13] J.P.C. Baena, L. Steier, W. Tress, M. Saliba, S. Neutzner, T. Matsui, F. Giordano, T.J. Jacobsson, A.R.S. Kandada, S.M. Zakeeruddin, A. Petrozza, A. Abate, M.K. Nazeeruddin, M. Grätzel, A. Hagfeldt, Highly Efficient Planar Perovskite Solar Cells Through Band Alignment Engineering, Energy Environ. Sci. 8 (2015) 2928-2934.

[14] M.C. Kao, H.Z. Chen, S.L. Young, Improved Energy Conversion Efficiency of TiO2 Thin Films Modified with Ta2O5 in Dye-sensitized Solar Cells, Jpn. J. Appl. Phys. 52 (2013) 01AD04.

[15] J.H. Choi, S.H. Kwon, Y.K. Jeong, I. Kim, K.H. Kim, Atomic Layer Deposition of Ta-doped TiO2 Electrodes for Dye-sensitized Solar Cells, J. Electrochem. Soc. 158 (2011)

[16] K. Lee, P. Schmuki, Ta doping for an Enhanced Efficiency of TiO2 Nanotube Based Dye-sensitized Solar Cells, Electrochem. Commun. 25 (2012) 11-14.

[17] J. Liu, H. Yang, W. Tan, X. Zhou, Y. Lin, Photovoltaic Performance Improvement of Dye-sensitized Solar Cells Based on Tantalum-doped TiO2 Thin Films, Electrochim. Acta 56 (2010) 396-400.

[18] R. Ghosh, Y. Hara, L. Alibabaei, K. Hanson, S. Rangan, R. Bartynski, T.J. Meyer, R. Lopez, Increasing Photocurrents in Dye Sensitized Solar Cells with Tantalum-doped Titanium Oxide Photoanodes Obtained by Laser Ablation, ACS Appl. Mat. Interfac. 4 (2012) 4566-4570.

[19] Q. Jiang, J. Gao, L. Yi, G. Hu, J. Zhang, Enhanced Performance of Dye-sensitized Solar Cells Based on P25/Ta2O5 Composite Films, Appl. Phys. A 122 (2016) 442.

[20] A.K. Chandiran, M.K. Nazeeruddin, M. Grätzel, The role of Insulating Oxides in Blocking the Charge Carrier Recombination in Dye-sensitized Solar Cells, Adv. Funct. Mater. 24 (2014) 1615-1623.

[21] M. Altomare, K. Lee, M.S. Killian, E. Selli, P. Schmuki, Ta-doped TiO2 Nanotubes for Enhanced Solar-light Photoelectrochemical Water Splitting, Chem. Eur. J. 19 (2013) 5841-5844.

[22] Y. Furubayashi, T. Hitosugi, Y. Yamamoto, K. Inaba, G. Kinoda, Y. Hirose, T. Shimada, T. Hasegawa, A transparent Metal: Nb-doped Anatase TiO2, Appl. Phys. Lett. 86 (2005) 1-3.

[23] T. Hitosugi, N. Yamada, S. Nakao, Y. Hirose, T. Hasegawa, Properties of TiO2-based Transparent Conducting Oxides, Phys. Stat. Solidi A 207 (2010) 1529-1537.

[24] T. Hitosugi, Y. Furubayashi, A. Ueda, K. Itabashi, K. Inaba, Y. Hirose, G. Kinoda, Y. Yamamoto, T. Shimada, T. Hasegawa, Ta-doped anatase TiO2 Epitaxial Film as Transparent Conducting Oxide, Jpn. J. Appl. Phys. 44 (2005) L1063-L1065.

[25] V.C. Anitha, A.N. Banerjee, S.W. Joo, Recent Developments in TiO2; as n- and p-type Transparent Semiconductors: Synthesis, Modification, Properties, and Energy-related Applications, J. Mater. Sci. 50 (2015) 7495-7536.

[26] S.M. Bawaked, S. Sathasivam, D.S. Bhachu, N. Chadwick, A.Y. Obaid, S. Al-Thabaiti, S.N. Basahel, C.J. Carmalt, I.P. Parkin, Aerosol Assisted Chemical Vapor Deposition of Conductive and Photocatalytically Active Tantalum Doped Titanium Dioxide Films, J. Mater. Chem. A 2 (2014) 12849-12856.

[27] P. Mazzolini, T. Acarturk, D. Chrastina, U. Starke, C.S. Casari, G. Gregori, A. Li Bassi, Controlling the Electrical Properties of Undoped and Ta-Doped TiO2 Polycrystalline Films via Ultra-Fast-Annealing Treatments, Adv. Electr. Mater. 2016 (2016) 1500316-15003169.

[28] P. Mazzolini, P. Gondoni, V. Russo, D. Chrastina, C.S. Casari, A. Li Bassi, Tuning of Electrical and Optical Properties of Highly Conducting and Transparent Ta doped TiO2 Polycrystalline Films, J. Phys. Chem. C 119 (2015) 6988-6997.

[29] P. Mazzolini, V. Russo, C.S. Casari, T. Hitosugi, S. Nakao, T. Hasegawa, A. Li Bassi, Vibrational-Electrical Properties Relationship in Donor-Doped TiO2 by Raman Spectroscopy, J. Phys. Chem. C 120 (2016) 18878-18886.

[30] O. Frank, M. Zukalova, B. Laskova, J. Kürti, J. Koltai, L. Kavan, Raman spectra of Titanium Dioxide (anatase, rutile) with Identified Oxygen Isotopes (16, 17, 18), Phys. Chem. Chem. Phys. 14 (2012) 14567-14572.

[31] S. Ito, T.N. Murakami, P. Comte, P. Liska, C. Grätzel, M.K. Nazeeruddin, M. Grätzel, Fabrication of Thin Film Dye Sensitized Solar Cells with Solar to Electric Power Conversion Efficiency over 10%, Thin Solid Films 516 (2008) 4613-4619.

[32] L. Kavan, M. Grätzel, S.E. Gilbert, C. Klemenz, H.J. Scheel, Electrochemical and Photoelectrochemical Investigation of Single-Crystal Anatase, J. Am. Chem. Soc. 118 (1996) 6716-6723.

[33] G. Boschloo, D. Fitzmaurice, Spectroelectrochemical Investigation of Surface States in Nanostructured TiO2 Electrodes, J. Phys. Chem. B 103 (1999) 2228-2231.

[34] M. Jankulovska, T. Berger, T.L. Villarreal, R. Gomez, A Comparison of Quantum-Size Anatase and Rutile Nanowire Thin Films: Devising Differences in the Electronic Structure from Photoelectrochemical Measurementsy, Electrochim. Acta 62 (2012) 172-180.

[35] M. Jankulovska, T. Berger, S.S. Wong, R. Gomez, T. Lana-Villarreal, Trap States in TiO2 Films Made of Nanowires, Nanotubes or Nanoparticles: An Electrochemical Study, ChemPhysChem 13 (2012) 3008-3017.

[36] L. Kavan, K. Kratochvilová, M. Grätzel, Study of Nanocrystalline TiO2 (Anatase) Electrode in the Accumulation Regime, J. Electroanal. Chem. 394 (1995) 93-102.

[37] T. Berger, T. Lana-Villarreal, D. Monllor-Satoca, R. Gomez, Charge Transfer Reductive Doping of Nanostructured TiO2 Thin Films as a Way to Improve Their Photoelectrocatalytic Performance, Electrochem. Commun. 8 (2006) 1713-1718.

[38] M. Zukalova, M. Bousa, Z. Bastl, I. Jirka, L. Kavan, Electrochemical Doping of Compact TiO_2 Thin Layers, J. Phys. Chem. C 118 (2014) 25970-25977.

[39] J. Idigoras, T. Berger, J.A. Anta, Modification of Mesoporous TiO2 Films by Electrochemical Doping: Impact on Photoelectrocatalytic and Photovoltaic Performance, J. Phys. Chem. C 117 (2013) 1561-1570.

[40] U.C. Lacnjevac, V.V. Radmilovic, V.R. Radmilovic, N.V. Krstajic, RuO2 Nanoparticles Deposited on TiO2 Nanotube Arrays by Ion-exchange Method as Electrocatalysts for the Hydrogen Evolution Reaction in Acid Solution, Electrochim. Acta 168 (2015) 178-190.

[41] F. Fabregat-Santiago, E.M. Barea, J. Bisquert, G.K. Mor, K. Shankar, C.A. Grimes, High carrier density in TiO2 nanotube, J. Am. Chem. Soc. 130 (2008) 11312-11316.

[42] Q. Wang, S. Ito, M. Grätzel, F. Fabregat-Santiago, I. Mora-Sero, J. Bisquert, T. Bessho, H. Imai, Characteristics of High Efficiency Dye-sensitized Solar Cells, J. Phys. Chem. B 110 (2006) 25210-25221.

[43] F. Fabregat-Santiago, I. Mora-Sero, G. Garcia-Belmonte, J. Bisquert, Cyclic Voltammetry Studies of Nanoporous Semiconductors. Capacitive and Reactive Properties of Nanocrystalline TiO2 Electrodes in Aqueous Electrolyte, J. Phys. Chem. B 107 (2003) 758-768.

[44] F. Fabregat-Santiago, G. Garcia-Belmonte, J. Bisquert, P. Bogdanoff, A. Zaban, Mott Schottky Analysis of Nanoporous Semiconductor Electrodes in Dielectric State Deposited on SnO2(F) Conducting Substrates, J. Electrochem. Soc. 150 (2003) E293-E298.

[45] M. Turion, J. Bisquert, P. Salvador, Flatband Potential of F:SnO2 in a TiO2 Dye-Sensitized Solar Cell: An Interference Reflection Study, J. Phys. Chem. B 107 (2003) 9397-9403.

[46] M. Kunst, T. Moehl, P. Wunsch, H. Tributsch, Optoelectronic Properties of SnO2 /TiO2 Junctions, Superlattices Microstruct. 39 (2013) 376-380.

[47] R. Van de Krol, A. Goossens, J. Schoonman, Mott-Schottky Analysis of Nanometer-Scale Thin-Films Anatase TiO2, J. Electrochem. Soc. 144 (1997) 1723-1727.

[48] F. Fabregat-Santiago, G. Garcia-Belmonte, I. Mora-Sero, J. Bisquert, Characterization of Nanostructured Hybrid and Organic Solar Cells by Impedance Spectroscopy, Phys. Chem. Chem. Phys. 13 (2011) 9083-9118.

[49] S. Kapusta, N. Hackerman, Capacitive Studies of the Semiconducting Properties of Passive Tin Electrodes, Electrochim. Acta 25 (1980) 949-955.

[50] M. Metikos-Hukovic, S. Omanovic, A. Jukic, Impedance Spectroscopy of Semiconducting Films on Tin Electrodes, Electrochim. Acta 45 (1999) 977-986.

[51] K. Minhova-Macounova, M. Klusackova, R. Nebel, M. Zukalova, M. Klementova, I.E. Castelli, M.D. Spo, J. Rossmeisl, L. Kavan, P. Krtil, Synergetic Surface Sensitivity of Photoelectrochemical Water Oxidation on TiO2 (Anatase) Electrodes, J. Phys. Chem. C 101 (2017) DOI: 10.1021/acs.jpcc.6b09289.

[52] B. Laskova, M. Zukalova, A. Zukal, M. Bousa, L. Kavan, Capacitive Contribution to Li-storage in TiO2 (B) and TiO2 (Anatase), J. Power Sourc. 246 (2014) 103-109.

[53] L. Kavan, J. Rathousky, M. Grätzel, V. Shklover, A. Zukal, Surfactant-Templated TiO2 (Anatase): Characteristic Features of Lithium Insertion Electrochemistry in Organized Nanostructures, J. Phys. Chem. B 104 (2000) 12012-12020.

[54] L. Kavan, R. Bacsa, M. Tunckol, P. Serp, S.M. Zakeeruddin, F. Le Formal, M. Zukalova, M. Grätzel, Multi-walled Carbon Nanotubes Functionalized by Carboxylic Groups: Activation of TiO2 (Anatase) and Phosphate Olivines (LiMnPO4; LiFePO4) for Electrochemical Li-storage, J. Power Sourc. 195 (2010) 5360-5369.